Diffuse interface model to simulate the rise of a fluid droplet across a cloud of particles

Lecrivain, G.; Kotani, Y.; Yamamoto, R.; Hampel, U.; Taniguchi, T.;

Originally published:

September 2018

Physical Review Fluids 3(2018)9, 094002

DOI: https://doi.org/10.1103/PhysRevFluids.3.094002

A diffuse interface model to simulate the rise of a fluid droplet across a cloud of particles

Gregory Lecrivain,[1,2,*] Yuki Kotani,[2] Ryoichi Yamamoto,[2] Uwe Hampel,[1,3] and Takashi Taniguchi[2,†]

[1] *Helmholtz-Zentrum Dresden-Rossendorf, Institut für Fluiddynamik, Bautzner Landstraße 400, 01328 Dresden, Germany*

[2] *Kyoto University, Department of Chemical Engineering, Kyoto 615-8510, Japan*

[3] *Technische Universität Dresden, AREVA-Stiftungsprofessur für Bildgebende Messverfahren für die Energie- und Verfahrenstechnik, 01062 Dresden, Germany*

(Dated: March 1, 2018)

A large variety of industrial and natural systems involve the adsorption of solid particles to the fluidic interface of droplets in motion. A diffuse interface model is here suggested to directly simulate the three-dimensional dynamics of a fluid droplet rising across a cloud of large particles. In this three-phase model the two solid-fluid boundaries and the fluidic boundary are replaced with smoothly spreading interfaces. A significant advantage of the method lies in the fact that the capillary effects, the three-phase flow hydrodynamics, and the inter-particle collisions are all resolved. We first report important numerical limitations associated with the inter-particle collisions in diffuse interface models. In a second stage the effect of the particle concentration on the terminal velocity of a rising fluid droplet is investigated. It is found that, in a quiescent environment, the terminal velocity of the rising the fluid droplet decreases exponentially with the particle concentration. This exponential decay is also confirmed by a simple rheological model.

Keywords: Diffuse interface model, rising droplet, particles at fluidic interface, direct numerical simulation, three phase flows.

I. INTRODUCTION

A large variety of systems involve the adsorption of solid particles to the fluidic interface of droplets in motion. Important industrial applications include the stabilisation of emulsions and foams [1], the armouring of droplets moving in capillary tubes [2], along with the recovery of mineral particles by rising gas bubbles [3, 4]. The encapsulation of oceanic air bubbles in a stabilising organic film of particles is also remarkable phenomenon, for which the addition of solid constituent drastically changes the dynamics of a natural binary fluid system [5]. The direct numerical simulation of such ternary systems is difficult. This can probably be attributed to the complexity of the mechanism itself, in which capillary effects, three-phase flow hydrodynamics, and inter-particle collisions are all intertwined. The majority of the developed three-phase models were used to primarily test the dynamics of a single particle trapped at a planar fluidic interface [6–8]. Some more complex simulations were also performed to study the re-arrangement of ellipsoidal particles initially placed at the fluidic interface of an immobile spherical droplet [9, 10]. When it comes to simulating the rise of a droplet across a cloud of particles, scarcity becomes apparent. Only a few attempts can be found in the literature. We cite for instance the work of Sasic *et al.* [11], in which a Volume-of-Fluid method was used to simulate the dynamics of micro droplet interacting with a cloud of settling particles. Aim of this work is the three-dimensional simulation of a rising fluid droplet in a multi-particle system. The fully resolved three-phase simulations are performed using a modified diffuse interface model [12], meaning that the fluidic boundary and the two solid-fluid boundaries are replaced with smoothly spreading interfaces. A number of formulations based on diffuse interface models were proposed in the past [13–16]. Yet none of them were used to simulate the a rise of three-dimensional droplet across a dense cloud of solid particles. After discussing the problems associated with the use of diffuse interface models in a multi particle system, the effect of particle concentration on the terminal velocity of a rising droplet is studied.

II. SIMULATION MODEL

A. Binary fluid mixture

Suppose a ternary system, in which a dispersed solid constituent representing the particle cloud is immersed in a binary fluid mixture. A schematic of the reference ternary system presently investigated is illustrated in Figure 1. The capital letter "S" is hereafter introduced to denote a quantity associated with the solid constituent. The field $\phi_{\rm S}(\mathbf{x},t)$, where $\mathbf{x}$ is the spatial coordinate and t the time, denotes for instance the volume fraction of the solid constituent. The binary fluid mixture separates into its two immiscible fluid constituents "A" and "B". The constituent A represents the host fluid and the constituent B the fluid inside the droplet. In a similar fashion, the two volume fractions $\phi_{\rm A}(\mathbf{x},t)$ and $\phi_{\rm B}(\mathbf{x},t)$ are also introduced. The separation of the bi-

* g.lecrivain@hzdr.de

† taniguch@cheme.kyoto-u.ac.jp

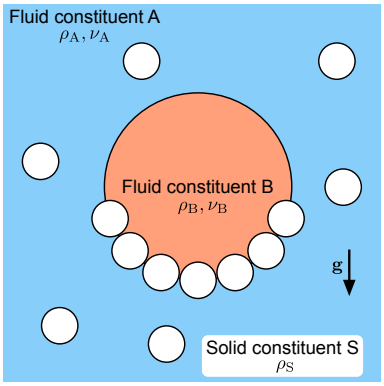

FIG. 1. Schematic of the reference ternary system representing a fluid droplet B rising in the host fluid A. The particles of the solid constituent S adsorb at the fluidic interface of the binary fluid.

nary fluid mixture into its two constituents is driven by the minimisation of the free energy

$$\mathcal{F} = \frac{k_B T_0}{v_0} \int_{\mathcal{V}} f(\phi_A, \phi_B, \phi_S)\, d\mathbf{x} \tag{1}$$

where $\mathcal{V}$ is the region of space occupied by the ternary system, k_B the Boltzmann constant, T_0 the temperature, v_0 a reference unit volume, and f the free energy density scaled by the reference value $e_0 = k_B T_0/v_0$. The formulation recently suggested by the same authors is here retained for the free energy density [17, 18]. The reader is referred to the Appendix A for its exact formulation. Because of the phase summation constraint $\phi_A + \phi_B + \phi_S = 1$ the free energy density is rewritten as $f(\psi, \phi_S)$, where this new order parameter is defined as $\psi(\mathbf{x}, t) = \phi_A - \phi_B$. This latter is updated in time according to the modified Cahn-Hilliard equation [14]

$$\frac{\partial \psi}{\partial t} + \nabla \cdot \Big[\psi \mathbf{u} - M\left(\mathbf{I} - \mathbf{n}_S \otimes \mathbf{n}_S\right) \cdot \nabla \mu\Big] = 0 \tag{2}$$

where M is the mobility, $\mathbf{I}$ the unit tensor, $\mathbf{n}_S = -\nabla\phi_S/|\nabla\phi_S|$ the local unit vector normal to the surface of the solid particle, and $\mu(\psi, \phi_S) = \delta\mathcal{F}/\delta\psi$ the chemical potential. Away from the particle diffuse interface the outer product $\mathbf{n}_S \otimes \mathbf{n}_S$ is set to the zero tensor.

B. Solid constituent

The solid particle cloud forming the solid constituent S is decomposed into a number N_S of spherical particles with identical radius r_S. The lower-case letter $s \in S$ is hereafter used to denote a quantity associated with the s-th Lagrangian particle. As one moves from the inner particle region to the outer region, the volume fraction ϕ_s of the s-th particle smoothly transition from unity to zero. A number of smooth profiles are suggested in reference [19]. A truncated hyperbolic function, associated with the interfacial distance ξ_S and the cut-off length ξ_c, is presently used to represent the spherical shape of each particle. The exact mathematical expression for $\phi_s(\mathbf{x}, t)$ can be seen in Eq. (B1) of the Appendix. Note that, the cut-off length is primarily introduced to speed up the calculation time. It reduces the number of times the hyperbolic function is called. The total volume fraction of the solid constituent is then given by

$$\phi_S(\mathbf{x}, t) = \sum_{s \in S} \phi_s. \tag{3}$$

C. Hydrodynamics

The total velocity field is resolved using the "smooth profile method", which essentially uses a Cartesian grid to solve the Navier-Stokes equations. In this method the total velocity field is decomposed as $\mathbf{u} = (1 - \phi_S)\mathbf{u}_{AB} + \phi_S \mathbf{u}_S$, where the first term is the velocity field of the binary fluid and the second term the solid velocity field. This latter is defined as $\phi_S \mathbf{u}_S = \sum \phi_s[\mathbf{V}_s + \boldsymbol{\Omega}_s \times (\mathbf{x} - \mathbf{X}_s)]$. Further reading on the smooth profile method can be found in the reference section [19, 20]. The total velocity, which satisfies the incompressibility condition $\nabla \cdot \mathbf{u} = 0$, is here given by solving the modified momentum equation

$$\rho\left[\frac{\partial \mathbf{u}}{\partial t} + (\mathbf{u} \cdot \nabla)\,\mathbf{u}\right] = \nabla \cdot [-p\mathbf{I} + \boldsymbol{\sigma}_v] + \rho\phi_S \mathbf{f}_S + \mathbf{f}_c + \mathbf{f}_g \tag{4}$$

where $\boldsymbol{\sigma}_v$ is the viscous stress tensor. The first additional term $\mathbf{f}_S$ on the right hand side of Eq. (4) enforces the particle rigidity. Its exact formulation can be found in the original development of the smooth profile method [19, 20]. The second capillary term is given by $\mathbf{f}_c = -\psi\nabla\mu - \phi_S\nabla\mu_S$, where $\mu_S = \delta\mathcal{F}/\delta\phi_S$ [17]. The third gravity term is given by $\mathbf{f}_g = (\rho - \rho_{avg})\mathbf{g}$. The substraction by the space averaged density $\rho_{avg} = \int\rho(\mathbf{x}, 0)d\mathbf{x}/\int d\mathbf{x}$ was previously suggested for buoyancy-driven droplet flows in a periodic domains [21]. The total density and viscosity fields are given by

$$\rho(\mathbf{x}, t) = \phi_A(\mathbf{x}, t)\rho_A + \phi_B(\mathbf{x}, t)\rho_B + \phi_S(\mathbf{x}, t)\rho_S \tag{5}$$

$$\eta(\mathbf{x}, t) = \phi_A(\mathbf{x}, t)\eta_A + \phi_B(\mathbf{x}, t)\eta_B + \phi_S(\mathbf{x}, t)\eta_S \tag{6}$$

where the constants $\rho_{i=A,B,S}$ and $\eta_{i=A,B,S}$ are the respective user-defined density and viscosity of each constituent.

D. Multi-particle dynamics

The hydrodynamic force $\mathbf{F}_{hyd}$, the capillary force $\mathbf{F}_{cap}$, the collision force $\mathbf{F}_{col}$, and an external force $\mathbf{F}_{ext}$ acting on each particle are presently retained. The equations for the translational velocity $\mathbf{V}_s = d\mathbf{X}_s/dt$, where $\mathbf{X}_s$ is

the position of the s-th particle centre of mass, and the rotational velocity $\mathbf{\Omega}_s$ are given by [22]

$$m_s \frac{\mathrm{d}\mathbf{V}_s}{\mathrm{d}t} = \mathbf{F}_{\mathrm{hyd}} + \mathbf{F}_{\mathrm{cap}} + \mathbf{F}_{\mathrm{col}} + \mathbf{F}_{\mathrm{ext}} \tag{7}$$

$$\mathbf{I}_s \frac{\mathrm{d}\mathbf{\Omega}_s}{\mathrm{d}t} = \mathbf{T}_{\mathrm{hyd}} + \mathbf{T}_{\mathrm{cap}} \tag{8}$$

where m_s is the particle mass, $\mathbf{I}_s$ the diagonal inertia tensor, $\mathbf{T}_{\mathrm{hyd}}$ the hydrodynamic torque, and $\mathbf{T}_{\mathrm{cap}}$ the capillary torque. The hydrodynamic and the capillary components are directly resolved. Their values are calculated by using a momentum conservation between the solid constituent and the binary fluid mixture. A detailed description of the force and torque calculations can be seen in the references [17, 18].

1. *Depletion layer adjacent to the particle boundary (S1)*

The reference system presently studied is composed of a binary fluid mixture, whose fluid constituents A and B are ideally separated by a sharp interface, and by multiple hard-sphere solid particles S with precise radii r_{S}. In this work, however, the three interfaces A/B, A/S, and B/S are no longer sharp but are replaced with smoothly spreading interfaces, whose thicknesses are user-defined (Figure 2). The thicknesses are here set to impose the surface energy. As one moves from the particle inner region to the host fluid constituent A, the order parameter ψ smoothly transitions from zero to unity. This leads to the formation of a depletion layer across the solid particle boundary (Figure 2a). In a multiple particle system, as

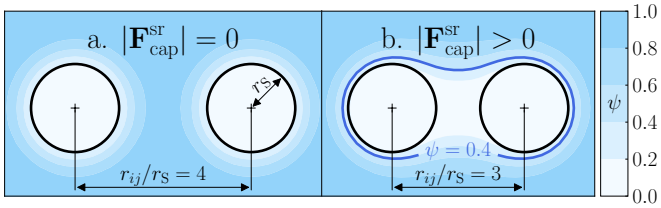

FIG. 2. Depletion layers adjacent to the boundaries of two solid particles immersed in the host consistent A (a). The two particles are pinned. Upon a close encounter, the depletion layers deform and the two particles attract each other because of a short-range capillary force $\mathbf{F}^{\mathrm{sr}}_{\mathrm{cap}}$ (b).

is the case here, this depletion layer might induce an undesired capillary attraction. As two particles come close to each other, their respective depletion layers tend to locally deform (Figure 2b). Subsequently, a short-range capillary force $\mathbf{F}^{\mathrm{sr}}_{\mathrm{cap}}$ arises. This scenario, reminiscent of the liquid bridge bonding particles together [23, 24], is an inevitable disadvantage occurring when working with a diffuse interface model. The distance, at which the short-range capillary force activates, has here a value comparable to that of the particle size and so an affordable computational cost is achieved. This short-range attraction distance could be further reduced by using a finer grid resolution and then setting a smaller ratio of the interfacial thickness to the particle radius ξ/r_{S}. Counteracting this short-range capillary attraction is a central aspect of this work. We here suggest to implement the repulsive collision force acting on the i-th particles as $\mathbf{F}_{\mathrm{col}} = -(\mathbf{F}^{\mathrm{sr}}_{\mathrm{cap}} + \nabla U_{ij})$, where $\mathbf{F}^{\mathrm{sr}}_{\mathrm{cap}}$ is calculated using a preliminary set of simulations (detailed in the result section) and U_{ij} is a truncated Lennard-Jones potential [25]. The potential takes the form

$$U_{ij} = \begin{cases} 4\epsilon \left[\left(\frac{\sigma}{r_{ij}}\right)^{12} - \left(\frac{\sigma}{r_{ij}}\right)^{6} \right] & \text{if } r_{ij} < r_c \\ 0 & \text{elsewhere} \end{cases} \tag{9}$$

where ϵ is the depth of the potential well, $r_{ij} = |\mathbf{X}_i - \mathbf{X}_j|$ the separation distance between the centre of masses of the i-th and the j-th particles, $\sigma = 2r_{\mathrm{S}} + \xi_c$ the distance at which the inter-particle potential equates zero, and $r_c = 2^{1/6}\sigma$ the cut-off distance. The truncation suppresses the attractive part of the potential.

III. RESULTS

The governing equations were implemented in their non-dimensional form using the Reynolds number Re, the Peclet number Pe, the capillary number Ca. These three non-dimensional numbers are defined as

$$\mathrm{Re} = \frac{\rho_0 U_0 L_0}{\eta_0}, \ \mathrm{Pe} = \frac{U_0 L_0}{D_0}, \ \mathrm{Ca} = \frac{\eta_0 U_0}{\gamma_0} \tag{10}$$

where $\rho_0 = \rho_{\mathrm{A}}$ and $\eta_0 = \eta_{\mathrm{A}}$ are the density and the viscosity of the host fluid constituent A. The reference velocity is set to $U_0 = \sqrt{gL_0}$. The reference length is defined as $L_0 = \xi$, the diffusion coefficient as $D_0 = e_0 M$, and the reference surface tension as $\gamma_0 = e_0 L_0$. This non-dimensionalisation is similar to that used in previous studies on phase separation [26, 27]. For the sake of conciseness, the procedure implemented to solve the governing equations is deliberately omitted. The detailed description is presented in references [17, 18]. The only difference is that a successive over-relaxation method is here employed to solve the Poisson equation. Note that this solver along with some of the discretisation schemes used in the advection Eq. (2) are not optimal. The implementation of more a advanced numerical procedure [28] is however well involved. Using the present implementation, a capillary number down to $\mathrm{Ca} = 10^{-2}$ and a fluid density ratio up to $\rho_{\mathrm{A}}/\rho_{\mathrm{B}} = 40$ can be achieved. The resulting droplet Reynolds and Eötvös numbers are calculated, based on the droplet radius r_b, as $\mathrm{Re}_b = \rho_{\mathrm{A}} r_b \sqrt{g r_b}/\eta_{\mathrm{A}} = 1.29$ and $\mathrm{Eo}_b = \rho_{\mathrm{A}} g r_b^2/\gamma_0 = 0.33$ for all subsequent simulations. These two numbers, commonly used to characterise the shape of rising gas bubbles in water [29], confirm that the rising droplet remains spherical throughout the simulations, thereby avoiding

	Binary fluid mixture						Solid constituent						Collision		Numbers			Grid	
	ξ_A/ξ	ξ_B/ξ	χ	ρ_A/ρ_B	η_A/η_B	r_b/ξ	ξ_S/ξ	ξ_c/ξ	ρ_S/ρ_A	η_S/η_A	r_S/ξ	N_S	σ/ξ	$\epsilon/(\gamma_0\xi^2)$	Pe	Re	Ca	Δ/ξ	N
S1	1	1	8/3	[1-40]	1	21.3	-	-	-	-	-	0	-	-	1	0.01	0.05	1	128^3
S2	1	1	8/3	-	-	-	3	3.6	1	1	5	2	13.6	0.5	1	0.01	0.05	1	128^3
S3	1	1	8/3	10	1	25.6	3	3.6	1	1	5	[0-100]	13.6	0.5	1	0.01	0.05	1	128^3
S4	1	1	8/3	10	1	25.6	3	3.6	1	1	5	[0-300]	13.6	0.5	1	0.01	0.05	1	128^3

TABLE I. Parameters used in the simulation sets. The term Δ is the size of a grid element and N the number of grid nodes.

the ellipsoidal bubble regime. All the subsequent results are presented for two-dimensional and three-dimensional test cases.

A. Rising droplet in the absence of particles (S1)

First the terminal velocity of a rising droplet in a periodic domain is validated (Simulation set S1). There are no particles in the system. The input parameters used in the simulation set S1 are shown in Table I. In the Stokes regime, i.e. at low droplet Reynolds and Eötvös numbers, the spherical droplet slightly deforms during its ascension. This allows us to compare the simulated droplet terminal velocity $\mathbf{U}_b^{\text{sim}} = \int \phi_B \mathbf{u} d\mathbf{x} \,/\, \int \phi_B d\mathbf{x}$ with its theoretical counterpart $\mathbf{U}_b^{\text{th}}$ [30, 31]. The derivation of the theoretical terminal droplet velocity is described in Appendix C. Figure 3 shows the error in the droplet terminal velocity as a function of the fluid density ratio. It is seen that a remarkable agreement is achieved for $\rho_A/\rho_B > 10$. An error below 5% is achieved in a two-dimensional domain. In a three-dimensional domain the error fall below 7%. Note that the error is also dependent on the interfacial thicknesses ξ, ξ_A, and ξ_B [19]. Although it not shown here, the deformation of the droplet was found to compare qualitatively well with the data of Hysing *et al.* [32] at higher Capillary numbers.

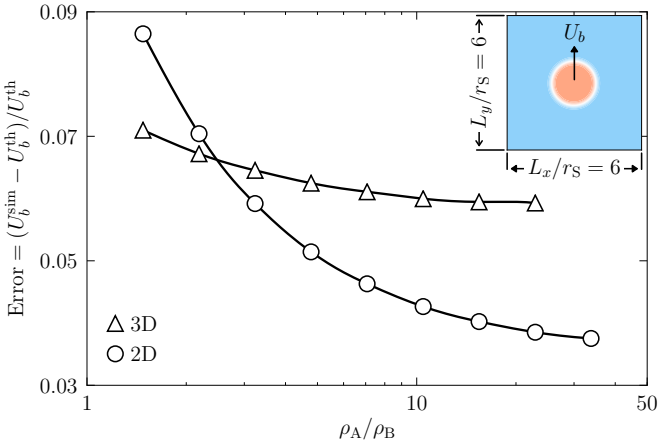

FIG. 3. Error in the terminal velocity of a rising spherical bubble in the absence of particles. Periodicity is enforced on all side boundaries of the domain.

B. Rising droplet in the presence of particles

1. Calculation of the short-range capillary force (S2)

At this stage the short-range capillary force $\mathbf{F}_{\text{cap}}^{\text{sr}}$ is still unknown. Hence a second of set of simulations S2, in which two pinned particles are immersed in the host fluid constituent A, is performed. As seen in Table I, the depth of the potential wall ϵ is arbitrarily set to a constant value throughout the subsequent simulations. Figure 4 shows the evolution of the short-range capillary force calculated as a function of the particle separation distance $r_{ij} - 2r_S$. It is seen that the short-range capillary force decays exponentially with the separation distance. This finding is in-line with previously reported data [14]. The magnitude of the repulsive force $-\nabla U_{ij}$, derived from the Lennard-Jones potential in Eq. (9), is also shown.

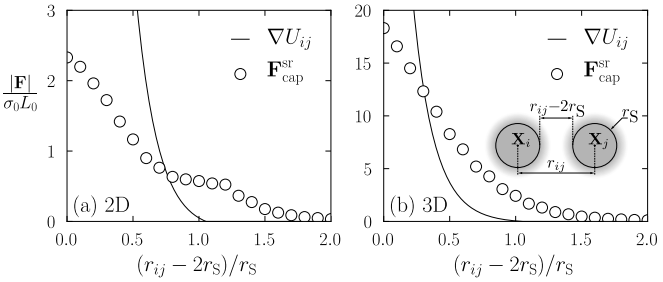

FIG. 4. Short-range capillary force $\mathbf{F}_{\text{cap}}^{\text{sr}}$ calculated as a function of the normalised particle separation distance r_{ij}. The two particles are pinned and immersed in the fluid constituent A. The repulsive force $-\nabla U_{ij}$ is also shown.

2. Suppression of the clustering effect (S3)

The effect of the corrected collision force $\mathbf{F}_{\text{col}} = -(\mathbf{F}_{\text{cap}}^{\text{sr}} + \nabla U_{ij})$ on a multi-particle system is here briefly tested in the simulation set S3. At the initial time $t = 0$, the particles are randomly placed in the host fluid constituent A and the droplet is placed at the centre of the domain. The particles have the same density as that of the host fluid, i.e. $\rho_S/\rho_A = 1$. Figure 5 shows the effect of the corrected collision force on a multi-particle

system. In case (a), the collision force is too weak to overcome the short range capillary force, hence particle clustering occurs. In case (b), the clustering is suppressed. As expected the particles are eventually collected at the fluidic interface of the rising droplet. After the rising droplet is completely armoured, the surrounding particles suspended in the host fluid constituent A circumvent the rising particle-droplet aggregate. It is seen that a small surface-to-surface particle separation distance persists throughout the simulation. This separation distance could be reduced by reducing the length of the interfacial thicknesses while increasing the grid resolution. But the price to pay would be a significant increase in the computational cost.

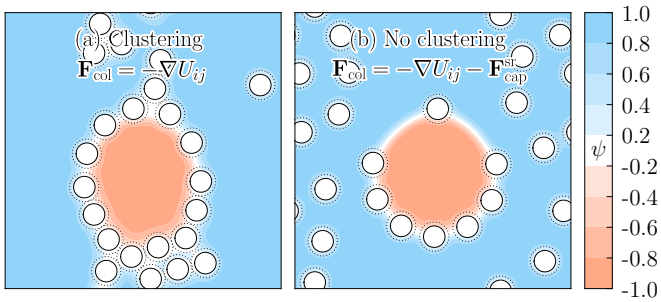

FIG. 5. Effect of the corrected collision force in a multi-particle system. In subfigure (a) clustering occurs as opposed to subfigure (b). The solid lines correspond to the reference particle radius $r_{\rm S}$ and the dashes lines to the collision radius $\sigma/2$ associated with the potential U_{ij}.

3. *Effect of particle concentration (S4)*

In the simulation set S4, the number of particles suspended in the domain is varied. Figure 6 shows the three-dimensional rising droplet at low total solid fraction (a) and at high solid fraction (b). An animation of the simulation can be found in the supplementary files. The fluidic interface of the droplet is defined as the iso-surface $\psi = 0$. The mean bubble velocity and its

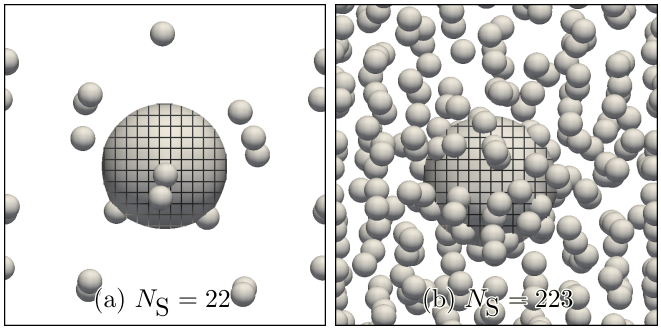

FIG. 6. Snapshot of the three-dimensional rising bubble in a multi-particle system. Sub-figure a: low particle concentration, sub-figure b: high particle concentration

deviation are then calculated as a function of the number of particles. The statistics are averaged over two flow-through times, with one flow-through time being the time it takes for the droplet to traverse the domain height. Figure 7 shows the terminal velocity of the rising droplet as a function of the solid concentration in the host fluid. The concentration of the solid constituent suspended in the host fluid, which essentially is a conversion of the number of particles suspended in A, is calculated as $\langle\phi_{\rm S}\rangle = \int\phi_{\rm S}{\rm d}\mathbf{x}/\int\phi_{\rm A}{\rm d}\mathbf{x}$. It is found that the terminal velocity U_b of the droplet decreases exponentially with increasing solid concentration. This decrease is backed up quantitatively by the recent numerical and experimental observations [33, 34]. For illustration purposes, an expo-

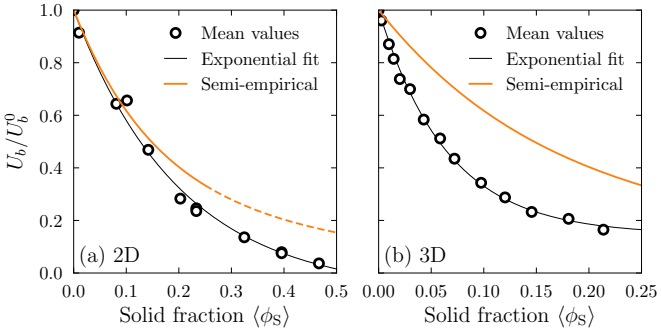

FIG. 7. Effect of the solid concentration in the host fluid on the terminal velocity of a rising bubble in the Stokes regime. The standard deviation of the mean bubble velocity is about as large as the symbols. The semi-empirical expression, obtained with $\lambda_0 = 4$ and $\lambda_1 = 12$, is extrapolated beyond its range of validity.

nential fit was added to the figure. The exponential fit takes the form $U_b/U_b^0 = 1-\alpha(1-e^{-\langle\phi_{\rm S}\rangle/\beta})$, where α and β are two best-fit values, and U_b^0 equates the terminal velocity of the droplet in the absence of particles. With the present best-fit function, the droplet velocity ratio equals unity for $\langle\phi_{\rm S}\rangle = 0$. With higher solid fraction, i.e. for $\langle\phi_{\rm S}\rangle \to 1$, the droplet terminal velocity converges to the constant value $U_b/U_b^0 = 1-\alpha$. In the present simulations, α equates a value close to unity. It may however take a greater value, should the bubble move down because of the gravity. A direct comparison with data taken from the literature is difficult because the few available studies consider the rising of highly deformable air bubbles in water [34]. The simulations are here performed with a smaller density ratio. Based on a the rheological model of Hooshyar *et al.* [33], we derive semi-empirical values for the terminal droplet velocity rising across a suspension of particles. In the semi-dilute regime, i.e. for $\langle\phi_S\rangle < 0.25$, the apparent viscosity of the suspension A/S takes the polynomial form

$$\frac{\eta_{\rm AS}}{\eta_{\rm A}} = 1 + \lambda_0\langle\phi_S\rangle + \lambda_1\langle\phi_S\rangle^2 \qquad (11)$$

where $1.5 < \lambda_0 < 5$ and $7.35 < \lambda_1 < 14.1$ [35]. In the dilute regime, restricted to $\langle\phi_S\rangle < 0.02$, the above

equation simplifies to the well established analytical expression $\eta_{\rm AS}/\eta_{\rm A} = 1 + 2.5\langle\phi_S\rangle$ [36]. By substituting the viscosity of the host fluid in Eq. (C1) with the apparent viscosity $\eta_{\rm AS}$, a semi-empirical terminal velocity can be estimated. While this semi-empirical value does not take into account the particle attachment to the fluidic interface of the rising droplet, it does confirm the exponential decay presently observed.

IV. CONCLUSIONS

A diffuse interface model was suggested to directly simulate the dynamics of a rising droplet in the presence of large particles. A significant advantage of the method lied in the fact that the capillary effects and the three-phase flow hydrodynamics were all resolved. An appropriate repulsive inter-particle collision force was suggested to counteract the short-range capillary attraction caused by the depletion layer adjacent to the particle boundary. This short-range capillary attraction, even though its effect can be diminished with a finer grid resolution, is inevitable when employing a diffuse interface model. In a second stage the effect of the particle concentration on the terminal velocity of a rising fluid droplet was investigated. It was found that, in the Stokes regime, the bubble terminal velocity decreases exponentially with the particle concentration. Further work will include an appropriate extension of the current model to achieve large density and viscosity ratios similar to those observed in industrial air-water systems.

ACKNOWLEDGMENTS

This work was supported by a Marie Curie International Outgoing Fellowship with the European Union Seventh Framework Program for Research and Technological Development (2007-2013) under the grant agreement number 623518.

Appendix A: Free energy density

This free energy density is given by

$$f = f_{\rm bulk} + \frac{\xi^2}{2}\left|\nabla(\phi_{\rm A} - \phi_{\rm B})\right|^2 + \frac{\xi_{\rm A}^2}{2}\left|\nabla(\phi_{\rm A} - \phi_{\rm S})\right|^2 + \frac{\xi_{\rm B}^2}{2}\left|\nabla(\phi_{\rm B} - \phi_{\rm S})\right|^2 \quad \text{(A1)}$$

where $f_{\rm bulk} = \phi_{\rm A}\ln(\phi_{\rm A}) + \phi_{\rm B}\ln(\phi_{\rm B}) + \chi\phi_{\rm A}\phi_{\rm B}$ is the bulk contribution and χ a parameter describing the affinity between the two fluid constituents. The three tunable interfacial length scales ξ, $\xi_{\rm A}$, and $\xi_{\rm B}$ preceding the gradient terms are introduced to control the particle wettability.

Appendix B: Smooth particle profile

The following mathematical function is used to represent the spherical shape of the s-th particle

$$\phi_s(\mathbf{x}) = \begin{cases} 1 & \text{if } |\boldsymbol{\ell}_s| < r_{\rm S} - \frac{\xi_c}{2} \\ 0 & \text{if } |\boldsymbol{\ell}_s| > r_{\rm S} + \frac{\xi_c}{2} \\ \frac{1}{2}\tanh\left(\frac{r_{\rm S} - |\boldsymbol{\ell}_s|}{\xi_{\rm S}/2}\right) + \frac{1}{2} & \text{elsewhere} \end{cases} \quad \text{(B1)}$$

where $r_{\rm S}$ is the particle radius, $\boldsymbol{\ell}_s(\mathbf{x}) = \mathbf{x} - \mathbf{X}_s$ the distance vector from the centre of mass $\mathbf{X}_s$ of the $s-$th particle to the spatial coordinate $\mathbf{x}$, and ξ_c the cut-off length.

Appendix C: Theoritical terminal bubble velocity

The theoretical terminal velocity $U_b^{\rm th}$ of a spherical bubble with radius r_b rising in a cubic periodic domain is calculated as

$$\frac{U_b^{\rm th}|_{\rm 3D}}{|\mathbf{F}_{\rm ext}|/(6\pi\eta_{\rm A} r_b)} = 1 - 1.7601c^{1/3} + c - 1.5593c^2 \quad \text{(C1)}$$

where $c = \int\phi_{\rm B}{\rm d}\mathbf{x}/\int{\rm d}\mathbf{x}$ is the fraction of space occupied by the bubble volume and $\mathbf{F}_{\rm ext} = (\rho_{\rm B} - \rho_{\rm A})\mathbf{g}\int\phi_{\rm B}{\rm d}\mathbf{x}$ is the external buoyancy force [30]. In a two-dimensional periodic square domain, the theoretical terminal velocity is given by

$$\frac{U_b^{\rm th}|_{\rm 2D}}{|\mathbf{F}_{\rm ext}|/(4\pi\eta_{\rm A} L_0)} = -0.5\log(c) - 0.738 + c \quad \text{(C2)}$$

The above expressions are valid for $c < 0.25$ [31].

[1] N. Taccoen, F. Lequeux, D. Gunes, and C. Baroud, Physical Review X **6**, 011010 (2016).
[2] Y. Yu, S. Khodaparast, and H. Stone, Soft Matter **13**, 2857 (2017).
[3] S. Tan, S. Ata, and E. Wanless, The Journal of Physical Chemistry B **117**, 8579 (2013).
[4] G. Lecrivain, G. Petrucci, M. Rudolph, U. Hampel, and R. Yamamoto, International Journal of Multiphase Flow **71**, 83 (2015).

[5] B. Johnson and C. R.C., Science **213**, 209 (1981).
[6] K. Stratford, R. Adhikari, I. Pagonabarraga, and J. C. Desplat, Journal of Statistical Physics **121**, 163 (2005).
[7] G. Davies, T. Kruger, P. Coveney, and J. Harting, Journal of Chemical Physics **141**, 154902 (2014).
[8] H. Mehrabian, J. Harting, and J. Snoeijer, Soft Matter **12**, 1062 (2016).
[9] T. Krüger, S. Frijters, F. Günther, B. Kaoui, and J. Harting, The European Physical Journal Special Topics **222**, 177 (2013).
[10] X. Luu and A. Striolo, Journal of Physical Chemistry B **118**, 13737 (2014).
[11] S. Sasic, E. Sibaki, and H. Ström, European Journal of Mechanics - B/Fluids **43**, 65 (2014).
[12] D. Anderson, G. McFadden, and A. Wheeler, Annual Review of Fluid Mechanics **30**, 139 (1998).
[13] T. Araki and H. Tanaka, Physical Review E **73**, 061506 (2006).
[14] H. Shinto, Advanced Powder Technology **23**, 538 (2012).
[15] P. Millett and Y. Wang, Journal of Colloid and Interface Science **353**, 46 (2011).
[16] T. Cheng and Y. Wang, Journal of Colloid and Interface Science **402**, 267 (2013).
[17] G. Lecrivain, R. Yamamoto, U. Hampel, and T. Taniguchi, Physics of Fluids **28**, 083301 (2016).
[18] G. Lecrivain, R. Yamamoto, U. Hampel, and T. Taniguchi, Physical Review E **95**, 063107 (2017).
[19] Y. Nakayama and R. Yamamoto, Physical Review E **71**, 036707 (2005).
[20] J. Molina and R. Yamamoto, Journal of Chemical Physics **139**, 1 (2013).
[21] A. Esmaeeli and G. Tryggvason, Physics of Fluids **17**, 093303 (2005).
[22] G. Lecrivain, R. Rayan, A. Hurtado, and U. Hampel, Computers & Fluids **124**, 78 (2016).
[23] G. Bournival, S. Ata, and E. Wanless, Advances in Colloid and Interface Science **225**, 114 (2015).
[24] X. Sun and M. Sakai, Physical Review E **94**, 063301 (2016).
[25] D. Bolintineanu, G. Grest, J. Lechman, F. Pierce, S. Plimpton, and P. Schunk, Computational Particle Mechanics **1**, 321 (2014).
[26] R. Chella and J. Vinals, Physical Review E **53**, 3832 (1996).
[27] V. Badalassi, H. Ceniceros, and S. Banerjee, Journal of Computational Physics **190**, 371 (2003).
[28] M. Fujita, O. Koike, and Y. Yamaguchi, Journal of Computational Physics **281**, 421 (2015).
[29] M. Tripathi, K. Sahu, and R. Govindarajan, Nature Communications **6**, 6268 (2015).
[30] H. Hasimoto, Journal of Fluid Mechanics **5**, 317 (1959).
[31] A. Sangani and A. Acrivos, International Journal of Multiphase Flow **8**, 343 (1982).
[32] S. Hysing, S. Turek, D. Kuzmin, N. Parolini, E. Burman, S. Ganesan, and L. Tobiska, International Journal for Numerical Methods in Fluids **60**, 1259 (2009).
[33] N. Hooshyar, J. van Ommen, P. Hamersma, S. Sundaresan, and R. Mudde, Physycal Review Letters **110**, 244501 (2013).
[34] M. Baltussen, J. Kuipers, and N. Deen, Chemical Engineering Science **158**, 561 (2017).
[35] S. Mueller, E. W. Llewellin, and H. M. Mader, Proceedings of the Royal Society of London A **466**, 1201 (2010).
[36] A. Einstein, annalen der Physik **34**, 591 (1911).